Advanced Laboratory Course
E217: STYX

Amelia Carina de Lope Fend, Martin Ludwig

07.05.2025

Contents

1. Introduction

Gaseous detectors form a large class of detectors that recognize incoming radiation through the ionization of gas. In addition to solid-state detectors, such as semiconductor or scintillation detectors, they are an essential component of modern particle physics experiments. Straw detectors are a specific type of gaseous detectors consisting of many gas-filled straw tubes, which enable track reconstruction of penetrating particles.

The Straw Tube Young student eXperiment (STYX) is a simple experiment comprising multiple layers of straw tubes, sandwiched between two scintillators for triggering. It is designed to demonstrate the working principle, setup, and calibration of a straw detector. In particular, the STYX detector is used to perform an overnight measurement of cosmic muons and analyze the data using the particle physics analysis framework ROOT.

This report is structured as follows: Chapter 2 provides a general description of the experimental setup, as well as explanations of the working principles of the detectors used. Chapter 3 describes the preparation of the setup, including the determination of the optimal operating voltages for the photomultiplier tubes and appropriate thresholds for the front-end electronics boards. After determining the optimal settings, an overnight measurement of cosmic muons was performed, the analysis of which is described in Chapter 4. Specifically, a straw-by-straw calibration was applied, tracks were reconstructed, and the angular distribution of the tracks, as well as the efficiency and noise rate of the straws, were studied. Finally, Chapter 5 summarizes the main results of this experiment.

2. Experimental Setup

This chapter provides a brief description of the STYX setup, a photo of which is shown in Figure 2.1. It consists of three drift chamber modules, described in Section 2.1, and two scintillators for triggering, described in Section 2.2. Unless stated otherwise, the presented information is taken from [1].

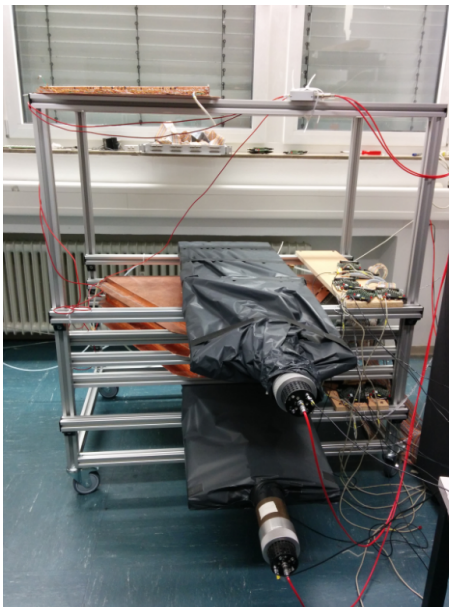

Figure 2.1.: STYX setup, including the copper-colored drift chamber modules and the black scintillator panels of the trigger system. Picture taken from [1].

2.1. Drift Chamber Setup

The STYX detector consists of three drift chamber modules. Each module, in turn, has three layers, and each layer is composed of 88 cylindrical straw tubes, each with a radius of 3.75 mm. Originally, the modules were part of the forward tracking system of the ZEUS detector at DESY, which is why they have a trapezoidal shape, with straw lengths ranging from 20 cm to 102 cm.

Each straw is filled with a gas mixture of argon and carbon dioxide and contains a thin wire at its center. The wire is held at high voltage, creating a radially symmetric electric field that is strongest near the wire. When an ionizing particle produces electron-ion pairs in the gas, the electrons drift rapidly toward the anode wire, while the ions move

toward the wall of the straw (cathode). Close to the anode wire, the electrons gain enough energy to ionize additional gas atoms. This leads to an avalanche, which induces an electric pulse on the wire.

The pulse is first processed by the front-end (FE) electronics, where every eight straws are connected to a single ASDQ chip. These chips contain amplifiers, shapers and discriminators, and they convert the analog pulse into a digital output signal if it exceeds a certain threshold. This threshold can be set at the FE boards. A proper threshold choice is crucial for achieving a good signal-to-noise ratio and is one of the goals of this experiment (see Section 3.2).

2.2. Trigger System and Data Acquisition

Constantly reading out the FE boards would result in large data streams containing many uninteresting events. Consequently, we need a way to determine an appropriate time for the detector readout. This is achieved using two scintillator panels located above and below the drift chamber modules. The panels emit scintillation light when an ionizing particle (e.g. a cosmic muon) passes through them.[1]

This light signal is very faint but can be detected using a photomultiplier tube (PMT). The first part of the PMT is a photocathode, from which incoming photons release electrons via the photoelectric effect. These electrons are subsequently multiplied by a series of electrodes (so-called dynodes). Between each pair of dynodes, electrons are accelerated by a voltage difference and release additional electrons upon striking the next dynode. In this way, a single initial electron is multiplied exponentially and can be measured as a pulse at the final anode. The voltage applied between the dynodes determines the gain and affects the number of detected events. The determination of an optimal PMT operating voltage is described in Section 3.1.

To trigger the readout cycle, the STYX setup requires a coincidence signal from both scintillators. This means that a muon must be detected in both the top and bottom panels almost simultaneously.[2] To reduce the number of output channels, the signals from six straws are time-multiplexed, meaning that they are attached with a relative delay of 200 ns. Accordingly, the total readout window per event is 1200 ns.

Before the readout data is sent to the lab PC, the timing of the straw pulses is measured and digitized using a time-to-digital converter (TDC). Finally, the raw data undergoes preprocessing by the provided `StyxM2C2` program. This includes merging signals into hits, removing unphysical pulses, and assigning proper time and position values to the hits.

[1] The exact scintillation mechanism depends on the type of radiation and the scintillator material (organic or inorganic). For our purposes, it is sufficient to know that the emitted light typically lies in the UV range and that the light yield is proportional to the deposited energy.

[2] The time muons need to travel through the detector is on a similar order as the setup's temporal resolution.

3. Preparation of the Setup

Before conducting any physical measurements, the setup must be prepared appropriately. First, we check whether the gas system is functioning properly. For this purpose, a bubbler is used to visualize the gas flow. Ideally, one should see a bubble every few seconds. After confirming this, we proceed with determining the optimal operating voltages of the PMTs, as described in Section 3.1. Finally, an appropriate threshold voltage for the FE boards must be found, which is presented in Section 3.2.

3.1. Determination of the PMT Operation Voltage

To find the optimal setting for the PMT voltages, we measure how the hit rates change as the voltage is varied. For this purpose, we refer to the three counters included in the setup. These display the number of hits in the upper and lower panels, as well as the number of coincidences that occur within a 10 s interval.

In general, we expect the number of detected hits to increase with increasing PMT voltage. At low voltages, the gain is small, meaning that not every scintillation light pulse produces a detectable signal at the anode. As the voltage increases, we expect the gain to rise exponentially until nearly all real scintillation events are detected. Further increasing the PMT voltage does not significantly increase the number of detected hits anymore. Instead, it causes the PMT to become more sensitive to electronic noise. We therefore search for the point at which the measured hit rate transitions from an exponential to a linear increase.

To find this value, we begin by varying the voltage of the bottom PMT in the range from 1700 V to 2300 V in steps of 50 V. For each voltage, we read off the detected hit rate. To obtain sufficient statistics, we take six measurements per voltage setting. The voltage of the upper panel is held constant at 1700 V during this measurement. The resulting data is listed in Table A.1.

From the six measurements, we compute the sample mean $\bar{N}$. Assuming Poisson errors $\sqrt{N}$, we estimate the uncertainty on the average hit rate as $\sigma_{\bar{N}} = \sqrt{\bar{N}}/\sqrt{6}$. Now we plot the average number of hits per 10 s as a function of the applied PMT voltage. The result is shown in Figure 3.1.

As expected, we observe an exponential increase in the number of detected hits, followed by an almost constant region. The last few data points exhibit a small linear increase. The transition occurs approximately at 2050 V. Accordingly, we choose this voltage as the optimal setting for the bottom PMT.

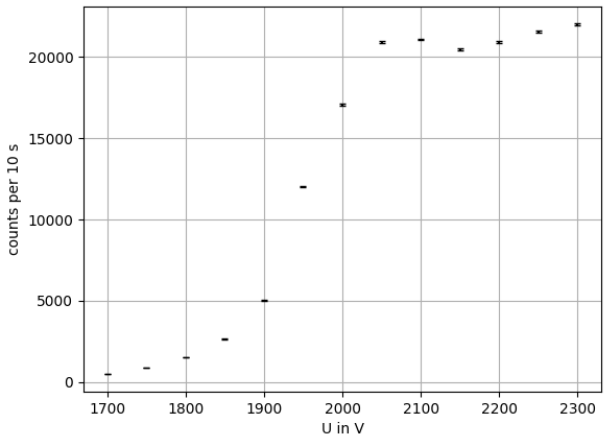

Figure 3.1.: Average number $\bar{N}$ of detected hits in the bottom panel as a function of the applied PMT voltages.

To find the optimal setting for the upper panel, we observe how the coincidence rate is affected when varying the upper PMT voltage. This time we expect it to first rise linearly before eventually reaching a plateau. The optimal setting is a voltage at the beginning of the plateau.

We keep the lower PMT voltage at the optimal value determined above and vary the upper PMT voltage over the same interval, from 1700 V to 2300 V, in steps of 50 V, again taking six measurements at each value. The resulting data are listed in Table A.2. The

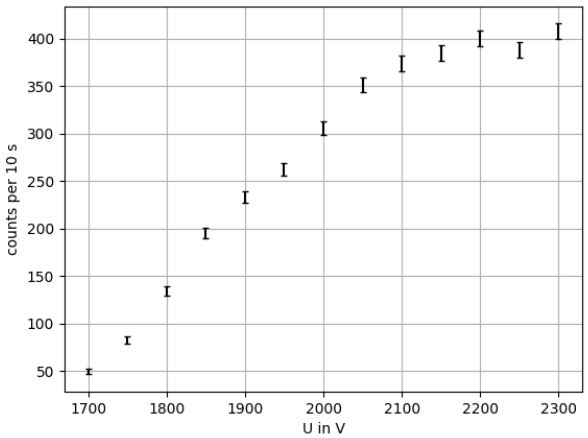

Figure 3.2.: Changes in the coincidence rate under variation of the upper panel PM voltage.

average count rates and their uncertainties were calculated as before and are plotted in Figure 3.2.

It can be seen that the detected counts initially increase linearly before the curve flattens. Since the last four data points are nearly consistent within their error bars, we assume that the plateau region begins at 2150 V. Accordingly, we use this voltage as the final setting for the upper PMT.

3.2. Determination of the FE Threshold Voltage

The FE boards require a reference voltage for the discriminators in the ASDQ chips, which is provided by a power supply. The power supply voltage does not directly correspond to the discriminator threshold voltage, however, a linear relation between them can be assumed.

Our aim in this part of the experiment is to determine the optimal setting for the FE threshold voltage. If it is set too low, a lot of noise will be processed by the ASDQ chips, contaminating the signal. If, on the other hand, it is set too high, real events may also be discarded. A good setting is a compromise between the two.

To find this optimal setting, we conduct six measurements in which we vary the voltage at the power supply from 1.4 V to 2.6 V, in steps of 0.3 V. Each time, we record 25 000 events. After preprocessing the recorded data with `StyxM2C2`, we examine individual channels and TDCs. Each channel contains the multiplexed signal of six straws. For a meaningful comparison between different threshold settings, we must find a channel in which all straws function properly. To this end, we generate two-dimensional histograms displaying the time and channel of raw hits in a TDC. An example is shown in Figure 3.3.

While most channels show hits every 200 ns, as expected, there are some channels (especially in TDC 0) where hits occur continuously. This indicates that the multiplexing or demultiplexing is not functioning properly. Additionally, there are several channels where hits are missing at multiples of 200 ns, which likely means that the corresponding straws are dead, meaning they do not detect anything at all.

Based on the plots shown in Figure 3.3, we decide to take a more detailed look at channel 22 of TDC 0.

Using `StyxThresholdScan`, we generate a rate plot that displays the total number of hits in the selected channel for each voltage setting. This is shown in Figure 3.4a. It can be seen that the number of counts initially decreases and then remains nearly constant starting from 2.0 V. A similar behavior is observed in the overlay plot (Figure 3.4b), which shows the multiplexed signals for each voltage (resulting in six peaks, each separated by 200 ns). Although the lines are difficult to distinguish and the statistics per straw are rather poor, the blue, green, and yellow lines (corresponding to 2.0 V, 2.3 V, and 2.6 V, respectively) generally lie below the black 1.4 V and red 1.7 V lines.

This implies that a threshold voltage of 2.0 V suppresses most of the background without significantly removing true signals. Accordingly, we choose 2.0 V as the optimal threshold setting for the FE boards.

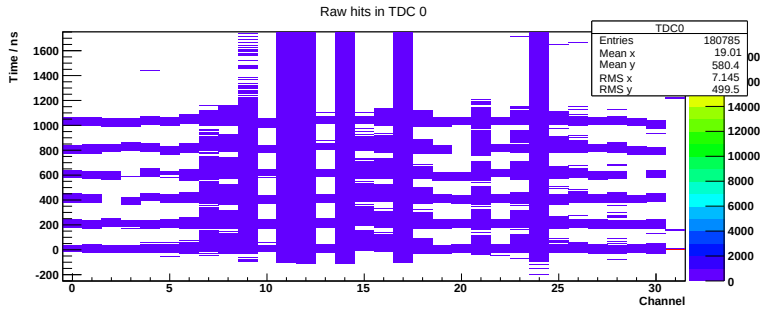

(a) TDC 0

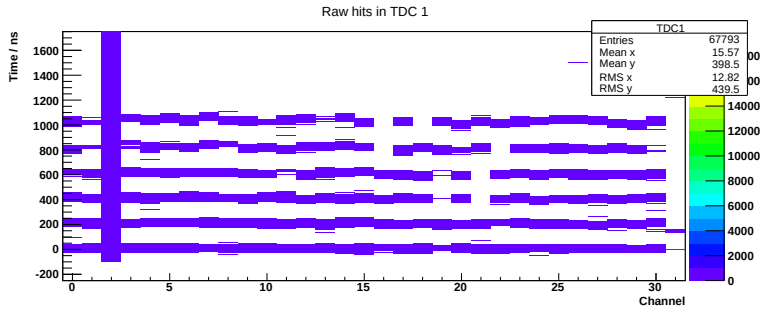

(b) TDC 1

Figure 3.3.: Two-dimensional histograms showing the time and channel number of raw hits in TDC 0 and TDC 1, both at a FE voltage of 2.0 V. The histograms for TDC 3 and TDC 4 are not depicted here, as they look similar.

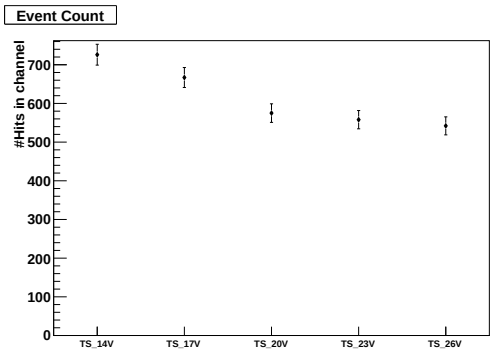

(a) Total number of hits

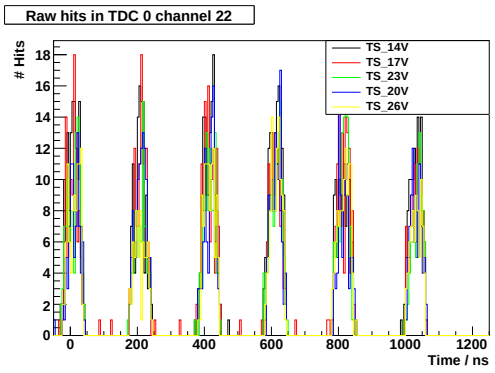

(b) Number of hits per time

Figure 3.4.: Total hit rate and overlay plot for TDC 0, channel 22. A higher FE threshold voltage reduces the number of detected hits. In this and the following plots, '14V' refers to 1.4 V and so on.

Since the FE threshold is set globally, but we have only investigated one specific channel so far, we should confirm our choice by examining additional channels. Based on Figure 3.3, we identify channel 10 of TDC 0 and channel 9 of TDC 1 as further suitable candidates. The rate and overlay plots for these channels are shown in Figures 3.5 and 3.6. In both cases, we observe a behavior very similar to that in Figure 3.4, indicating that 2.0 V is indeed a good setting for the majority of channels.

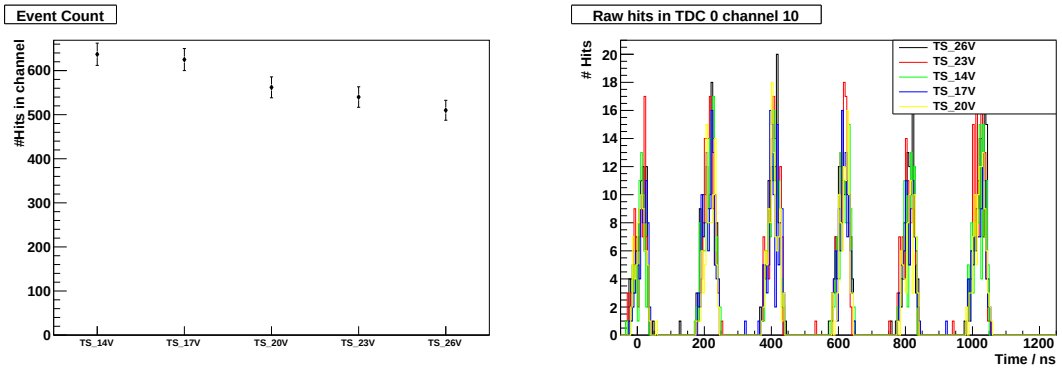

(a) Total number of hits (b) Number of hits per time

Figure 3.5.: Total hit rate and overlay plot for TDC 0, channel 10.

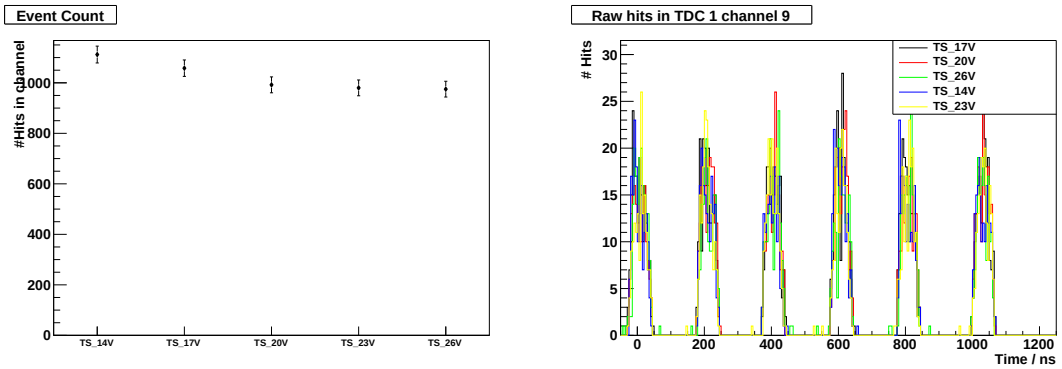

(a) Total number of hits (b) Number of hits per time

Figure 3.6.: Total hit rate and overlay plot for TDC 1, channel 9.

Finally, we examine the effect of the threshold by comparing the two dimensional histograms showing raw hits per channel per time for a fixed TDC for the chosen threshold voltage and the lowest threshold voltage. This is shown in Figure 3.7.

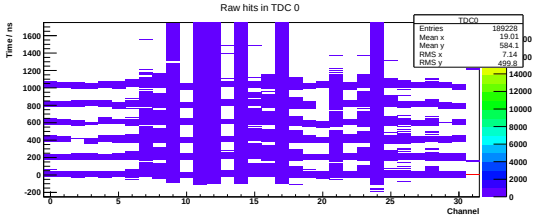

(a) Raw hits in TDC 0 at 1.4 V

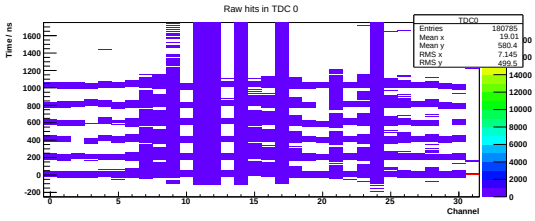

(b) Raw hits in TDC 0 at 2.0 V

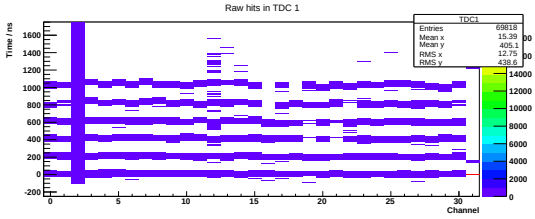

(c) Raw hits in TDC 1 at 1.4 V

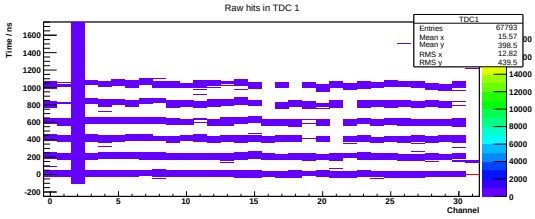

(d) Raw hits in TDC 1 at 2.0 V

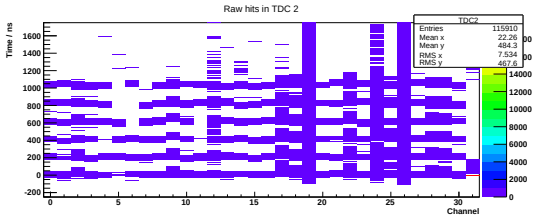

(e) Raw hits in TDC 2 at 1.4 V

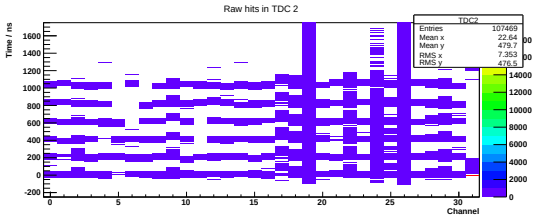

(f) Raw hits in TDC 2 at 2.0 V

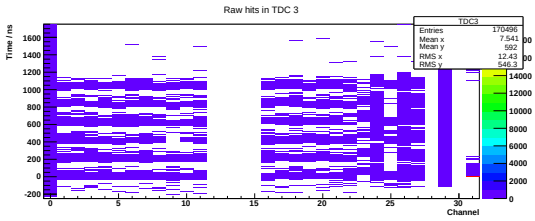

(g) Raw hits in TDC 3 at 1.4 V

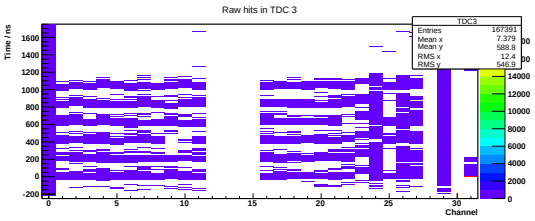

(h) Raw hits in TDC 3 at 2.0 V

Figure 3.7.: 2D histogram showing the raw hits in all TDCs in dependence of channel and time at lowest threshold voltage 1.4 V and chosen threshold voltage 2.0 V.

For each TDC, there are some hits outside of the times where we expect the multiplex signal from the straws, however the number of these is reduced when comparing the lowest voltage to the chosen threshold voltage. The signal at the expected times appears unchanged. This suggests that we succeeded in cutting out some of the noise without cutting into the signal.

3.3. Overnight Measurement

After determining the optimal operating voltage for the PMTs and an appropriate FE threshold voltage, we perform an overnight measurement to obtain a large data set. As

described in the following chapter, we use part of this data for calibration and the rest for analysis.

4. Analysis

Before a physically meaningful analysis of the recorded data from the overnight measurement can be conducted, it is necessary to perform a data calibration. The aim of this calibration is to adjust the straws' drift time distributions and to detect and flag faulty straws. Both steps are essential for the subsequent track reconstruction. For the calibration, we use the straw-by-straw method, whose application and results are described in Section 4.1. After calibration, the recorded data can be analyzed with respect to the distribution of hits in the detector, the angular distribution of reconstructed tracks, and the efficiency and noise rate of individual straws. This procedure is presented in Section 4.2.

4.1. Straw-by-Straw Calibration

For the calibration, we use the first 300 000 events from the overnight measurement. Again, these events must first be preprocessed using `StyxM2C2`, after which the calibration can be performed using the `StyxCalibration` program with the `CalibStrawByStraw` algorithm. The calibration corrects time offsets between signals coming from the FE board by aligning the drift time distributions of each straw. Additionally, it identifies non-functional straws and classifies them into three categories: *dead* straws, which show no signal at all; *hot* straws, which fire randomly; and *continuous* straws, which fire all the time.

Figure 4.1 visualizes the effect of the calibration. For each module, the drift time distribution of registered hits in the first (bottom) layer is displayed. The plots on the left-hand side show the status prior to calibration, while those on the right-hand side show the calibrated distributions.

When comparing the histograms, several differences become apparent: the full-length stripes in the uncalibrated histograms, which are particularly present in the top and bottom module plots, disappear after calibration. These stripes originate from continuously firing straws, which are identified and excluded during the calibration. As a result, gaps appear in the histograms at positions corresponding to such faulty straws. Excluding faulty straws also significantly reduces the total number of entries in the post-calibration histograms.

In addition, the drift time distributions of the functional straws are noticeably shifted. Before calibration, the distributions are mostly centered around 100 ns to 120 ns and show slight variations from straw to straw. The calibration procedure aligns these distributions, shifting them to start at zero and peak at approximately 40 ns.

Figure A.1 in the Appendix provides an alternative perspective on the behavior ob-

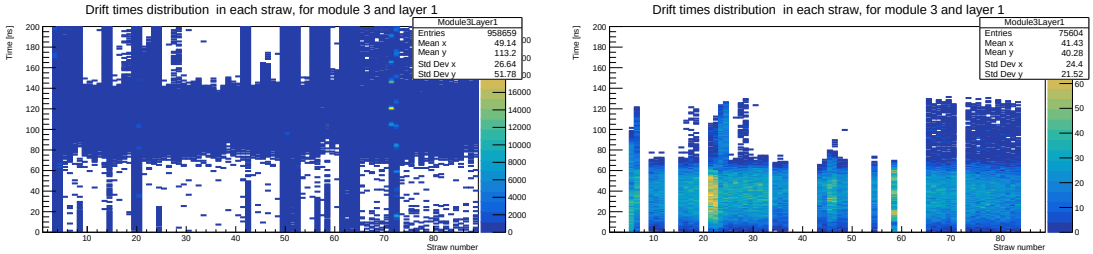

(a) Bottom layer of the top module

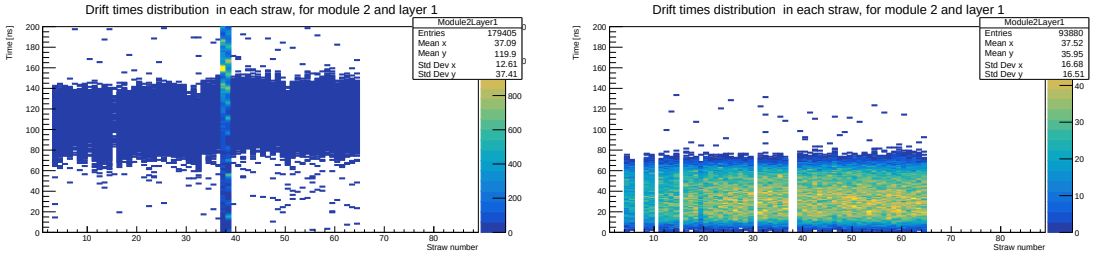

(b) Bottom layer of the middle module

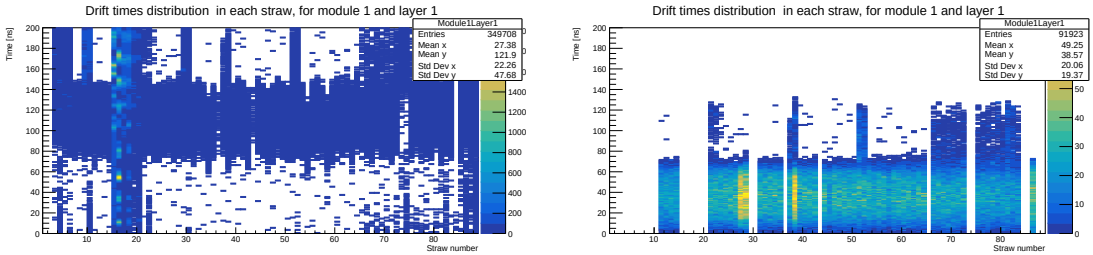

(c) Bottom layer of the bottom module

Figure 4.1.: Comparison of the drift time distribution in each straw of the bottom layer of each module. The plots on the left-hand and the right-hand side show the status before and after applying the calibration, respectively.

served in Figure 4.1. It essentially shows the y-projection of the histograms from Figure 4.1, but this time for the sum over all layers of each module rather than just the first layer. It can be seen that prior to calibration, the drift time distribution is dominated by several sharp peaks caused by continuously firing straws. After calibration, these peaks disappear, and the distribution transforms into a smooth curve, reflecting only the contributions from functional straws.

To summarize the performance status of each straw determined during the calibration, a straw mask is generated (see Figure 4.2). It displays each straw in its corresponding position within the detector and uses color coding (green, yellow, blue, and orange) to indicate properly working, dead, hot, and continuous straws, respectively. Table 4.1 lists

the total number of straws in each of these calibration categories. It shows that only about 65 % of all straws are properly functioning.

In the straw mask, it is striking that on the right side of the middle module, more than 20 straws in a row are dead in each layer. This means that this entire section does not detect any signals, as was already observed in Figure 4.1b. Additionally, it becomes apparent that, especially in the top and bottom modules, there are several clusters of hot straws. These conditions could lead to systematic errors in the subsequent track reconstruction, which should be kept in mind during the tracking analysis.

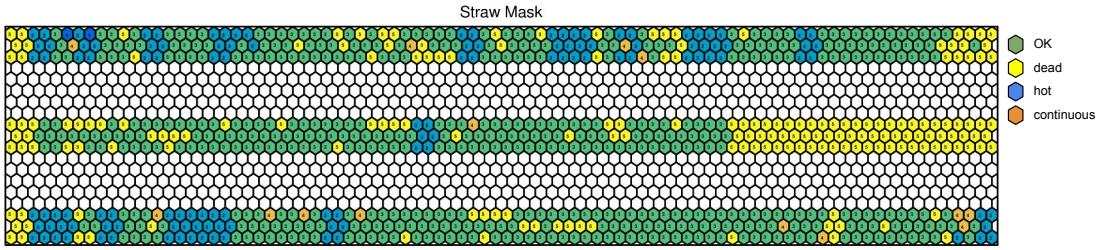

Figure 4.2.: Straw mask showing dead, hot and continuous straws. We edited the legend of the original file, as the labels for hot, dead and continuous did not match the drift time plots, so we assume there was an error.

Table 4.1.: Number of straws with a certain calibration status.

status	number of straws
OK	470
dead	112
hot	122
continuous	16

4.2. Tracking Analysis

After completing the calibration, we proceed with the analysis of the recorded data. For this analysis, we use 200 000 events from the overnight measurement that were not previously used for calibration, in order to avoid a bias. This time, for preprocessing, we run `StyxM2C2` with the generated calibration file, which contains the information about time alignment and faulty straws. In the following subsections, we examine the data with respect to the hit distribution inside the detector, the angular distribution of tracks, and the efficiency and noise rate of individual straws.

4.2.1. Hits per Straw

An interesting feature that is straightforward to study is the number of hits in each straw. This can be plotted for each layer or module, and the resulting histograms can

be compared to identify patterns in the hit distribution.

Figure 4.3 shows the number of hits in each of the three layers of the top module. As indicated in the straw mask (Figure 4.2), the histograms in Figure 4.3 contain gaps at positions corresponding to faulty straws, which are excluded from the analysis. Aside from that, the histograms appear very similar. This is the expected behavior, as adjacent straws should register a comparable number of hits. A similar overall pattern is observed in the other modules, with the corresponding plots shown in Figures A.2 and A.3 in the Appendix.

A general trend visible across all histograms is a decrease in the number of hits toward the edges of the detector. This is explained by the triggering mechanism: an event is only recorded if hits are registered in both scintillator panels. Since cosmic muons can travel not only vertically but also at angles (see Section 4.2.3), there are more possible trajectories through the central region. This leads to a higher hit rate in the central straws compared to the edges.

One might naively expect the length of the straws to affect the number of detected hits. However, because the scintillator panels have a fixed width, the sections of the longer straws that extend beyond the panel area do not contribute. Consequently, no clear linear relationship is observed between the straw number and the number of detected hits.

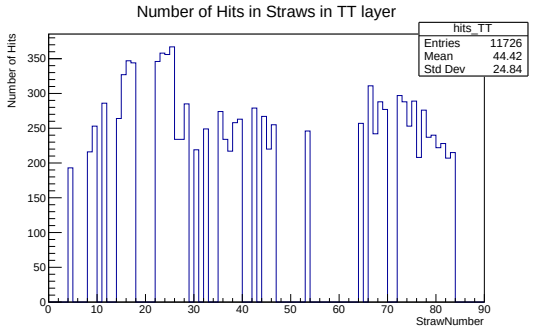

(a) Top layer, top module

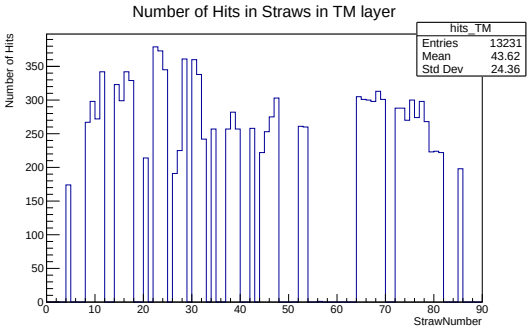

(b) Middle layer, top module

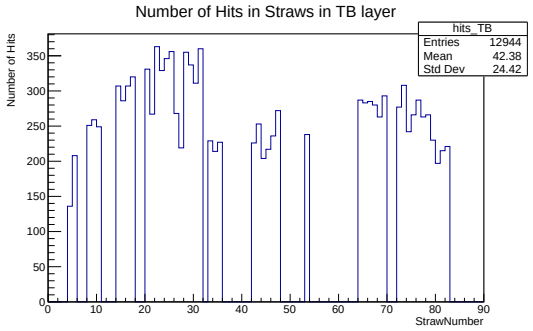

(c) Bottom layer, top module

Figure 4.3.: Hits per straw for each layer of the top module

We can also examine the number of hits per straw in each module, corresponding to the sum of the histograms from the individual layers. This is shown in Figure 4.4. Again, the shape of the histograms and the number of entries strongly depend on the distribution of faulty straws across the detector. For this reason, a direct comparison between modules is not meaningful. However, as observed previously for the individual layers, a trend toward fewer hits at the edges is still visible.

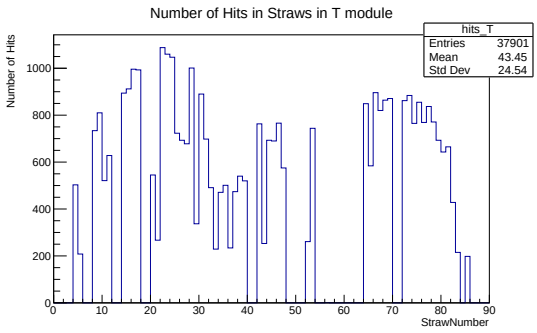

(a) Top module

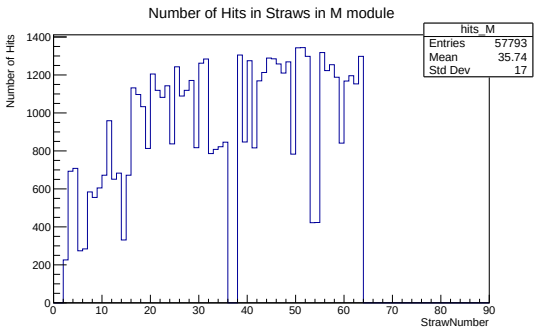

(b) Middle module

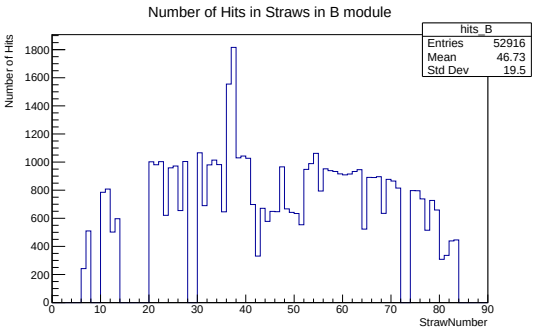

(c) Bottom module

Figure 4.4.: Hits per straw for each module

4.2.2. Tracks per Event

As part of the analysis, tracks in the detector are reconstructed. This means that a sequence of hits with appropriate temporal and spatial correlation is grouped together as a track. A natural question to ask is how many tracks occur per event and how this number relates to the number of hits per event. To answer this question, we can plot the number of tracks versus the number of hits in a two-dimensional histogram, as shown in Figure 4.5.

It can be seen that for most of the events (33 918 out of 50 000), no track could be reconstructed. If four or more hits were registered in the detector, it is likely that at least one track could be formed from them. However, events in which more than one track could be reconstructed are very rare (a total of 721 instances). Overall, a correlation

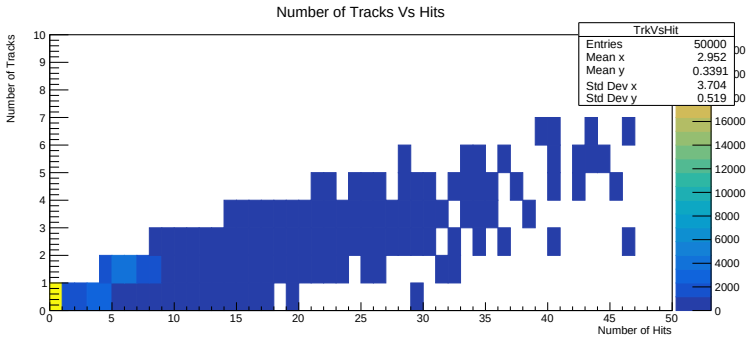

Figure 4.5.: Number of reconstructed tracks versus number of hits per event.

between the number of hits and the number of tracks is observable: a higher number of detected hits increases the likelihood of reconstructing one or more tracks.

4.2.3. Angular Distribution

The track reconstruction enables us to analyze the angular distribution of tracks. For cosmic muons, we expect the intensity I to depend on the zenith angle θ. Muons with larger angles travel a longer distance before reaching sea level and are therefore more likely to interact or decay. Theoretically, it can be shown that the muon intensity follows a sinusoidal distribution [2]:

$$I(\theta) = I_0 \cos^2(\theta). \tag{4.1}$$

To test this prediction, we select all events with exactly one reconstructed track and plot a histogram of the tracks' slopes. This is shown in Figure 4.6, with the slope angle given in radians. We then fit the function

$$N(\theta) = A \cdot \cos^n(\theta + \phi) \tag{4.2}$$

to the data using the least-squares method. According to Eq. 4.1, we expect $n = 2$ and $\phi = 0$. The fitted function is shown as a red line in Figure 4.6, and the fitted parameters are:

$$A = 368.7(42) \qquad n = 3.095(59) \qquad \phi = 0.0037(43)\,\text{rad}\,.$$

It can be seen that the fit describes the overall behavior of the data well. However, it is striking that the central bins contain more entries than expected, while bins near the turning points of the fitted function contain fewer entries than predicted.

The fit result for the angular shift ϕ is compatible with zero and therefore matches the theoretical expectation. However, the exponent n was determined to be 3.095(59), which deviates significantly (by $\sim 19\sigma$) from the theoretical prediction of $n = 2$. The most probable reason for this discrepancy is the presence of systematic uncertainties introduced by the experimental setup. As observed earlier, many straws are non-functional, and in particular, faulty straws are not evenly distributed throughout the detector but appear in clusters. This non-uniformity may cause tracks at certain angles to be more

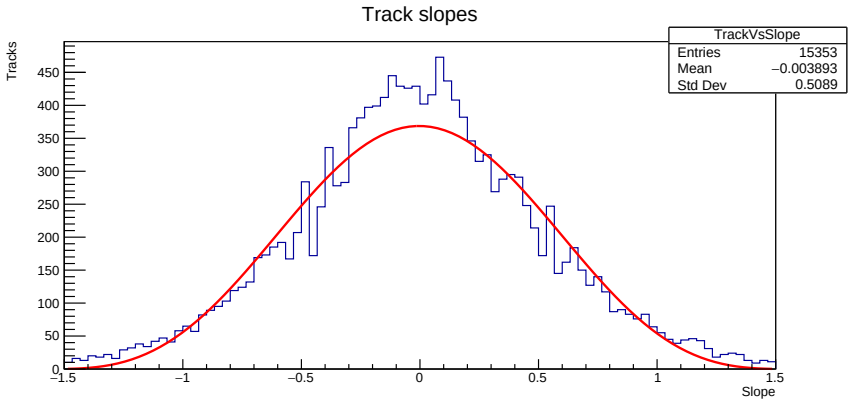

Figure 4.6.: Angular distribution of reconstructed tracks. The histogram was fitted according to Eq. 4.2 (red line). $\chi^2/\text{ndf} = 595/87$.

likely detected than others, ultimately leading to a systematic distortion of the angular distribution histogram. Additionally, as mentioned in Section 4.2.1 when discussing why straws on the edge of the detector registered fewer hits, due to the triggering mechanism, a track is only detected if its still fully covered by the detector, which is less likely for higher slopes. This geometrical effect also contributes to a higher exponent.

4.2.4. Efficiency and noise rate

As a final part of the analysis, we want to examine how well the functioning straws perform by studying their efficiency and noise rate.

We define the efficiency ϵ of a straw as the ratio between the number of detected hits N_h belonging to a track and the total number of expected hits. The latter is given by the sum of N_h and the number of "missing" hits N_mh, which refers to cases where a straw was penetrated by a reconstructed track but did not register a hit:

$$\epsilon = \frac{N_\text{h}}{N_\text{h} + N_\text{mh}}.$$

In terms of implementation, N_mh is determined by looping over all tracks and calculating the distance between the track and each straw. If the distance is smaller than the straw radius, the straw is considered to have been penetrated by the track.

Figure 4.7 shows the efficiency of each straw in a two-dimensional histogram. Well-performing straws should have an efficiency close to one. It can be seen that almost all straws have efficiencies greater than 50 %. The highest efficiencies are achieved in the middle module, where most straws reach 90 % or more. In the center of the top module, there is a region with relatively low efficiencies, only slightly above 50 %. In the bottom module, most values range between 70 % and 80 %.

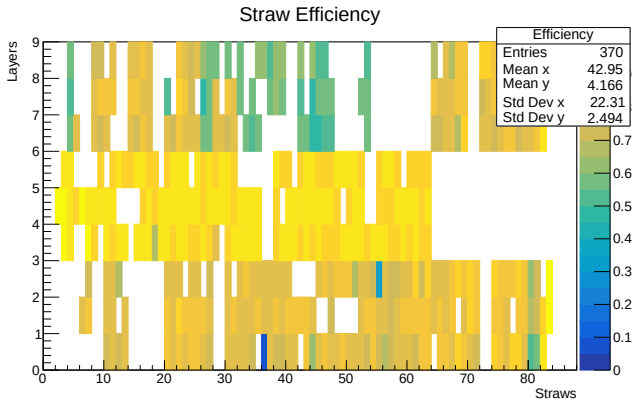

Figure 4.7.: Efficiency ϵ per straw.

Another measure of the straw performance is the noise rate ν. It is defined as the ratio between the number of noise hits N_n not belonging to any track and the total number of hits, $N_\mathrm{n} + N_\mathrm{h}$:

$$\nu = \frac{N_\mathrm{n}}{N_\mathrm{n} + N_\mathrm{h}}.$$

Figure 4.8 displays the calculated noise rates for each straw. Ideally, these values should be close to zero. Indeed, for most straws they lie between 10 % and 30 %.

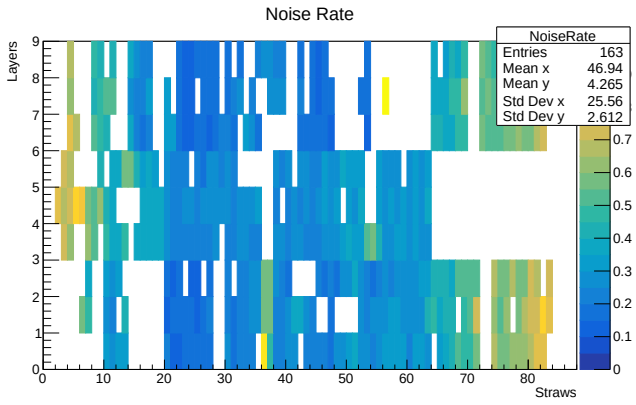

Figure 4.8.: Noise rate ν per straw.

In contrast to the efficiency, the noise rate depends on the straw position and gradually increases to over 70 % near the edges. The reason for this is that fewer tracks pass through the edges of the detector, reducing the chance of associating hits with valid tracks.

Additionally, there is one straw (number 57 in layer 8) with a noise rate of one. It does not appear in the efficiency plot, indicating that it detected no hits corresponding to a track. This may be due to a low number of properly functioning neighboring straws,

which reduces the likelihood of reconstructing tracks in that region. As a result, any noise hits detected by this straw lead to a noise rate of one. In this case, the high noise rate is likely due to low statistics in this part of the detector and may change if more events are analyzed.

5. Conclusion

Gaseous detectors are an essential component of modern particle physics experiments. Therefore, understanding their working principle, setup, and data analysis is crucial. The aim of the Straw Tube Young student eXperiment (STYX) was to impart basic knowledge about these topics.

In the first part of the experiment, the goal was to determine appropriate settings for the PMT operating voltages and the FE threshold voltages. The purpose of the PMTs is to convert the light from the scintillator panels used for triggering into electrical signals, with the operating voltage determining the gain. If the voltage is too low, not all light signals will be amplified. If it is too high, electronic noise will also be amplified. Thus, the optimal operating voltage lies in between. In our case, it was determined to be 2050 V for the bottom PMT and 2150 V for the top PMT.

The FE threshold voltage determines which signals from the straw tubes are processed and which are disregarded. To determine it, we conducted six measurements with voltages ranging from 1.4 V to 2.6 V. For each voltage, we examined the number of hits in various channels of different TDCs. By comparing the results, we concluded that 2.0 V is a suitable setting for the FE threshold voltage.

After preparing the setup, an overnight measurement was conducted, the calibration and analysis of which formed the main task of the second day. To correct time offsets between signals from the FE boards and to identify and flag faulty straws, a straw-by-straw calibration was performed.

After applying the calibration to the remaining data, we were able to analyze several properties of the reconstructed tracks. The distribution of hits per straw shows lower hit rates at the edges of the detector, which can be explained by the detector's triggering mechanism. When investigating how many tracks were reconstructed per event, we found that in only about 32 % of events, one or more tracks were reconstructed. Events with more than one reconstructed track were rare, and in general, the number of tracks per event increased with the number of hits contained in the event.

For the reconstructed events with exactly one track, we plotted their slopes to obtain the angular distribution of cosmic muons. While a $\cos^2$ dependence is expected from theory, we observed a $\cos^3$ behavior instead. We concluded that this deviation is mainly caused by the geometry of the detector setup and the presence of clusters of non-functional straws within the detector.

Finally, the efficiency and noise rate of the straws were computed. We observed that the efficiency is highest in the middle module, and that the noise rate is lowest in the center and increased toward the edges.

A. Appendix

A.1. Determination of the PMT Operation Voltage

Table A.1.: Detected hits N in the bottom scintillator for different applied PMT voltages. For each voltage setting, six measurements were taken, each lasting 10 s.

U / V	N_1	N_2	N_3	N_4	N_5	N_6
1700	522	503	463	458	520	474
1750	881	909	948	902	888	908
1800	1587	1564	1465	1550	1531	1497
1850	2700	2649	2695	2666	2600	2558
1900	4969	4896	4895	5230	5094	4992
1950	11915	12091	12147	11846	12017	12074
2000	17156	16955	17190	16889	17179	17104
2050	20804	21341	20966	21337	19693	21441
2100	20229	20221	21432	21226	21882	21507
2150	21610	20390	20365	20043	20178	20280
2200	20846	20922	20902	20936	20961	20898
2250	21314	21758	21425	21486	21624	21674
2300	22036	22117	21882	22160	21880	21852

Table A.2.: Detected coincidences N of both scintillators for different voltages applied to the upper PMT. For each voltage setting, six measurements were taken, each lasting 10 s.

U / V	N_1	N_2	N_3	N_4	N_5	N_6
1700	48	52	36	45	46	68
1750	95	76	99	81	64	80
1800	133	130	142	138	121	140
1850	209	193	206	199	189	176
1900	243	235	214	243	220	242
1950	238	255	251	269	273	285
2000	334	301	288	305	303	303
2050	373	350	352	335	336	360
2100	390	385	358	386	366	359
2150	402	344	395	382	385	401
2200	401	388	379	429	433	371
2250	359	370	401	389	405	403
2300	395	443	430	435	366	376

A.2. Straw-by-Straw Calibration

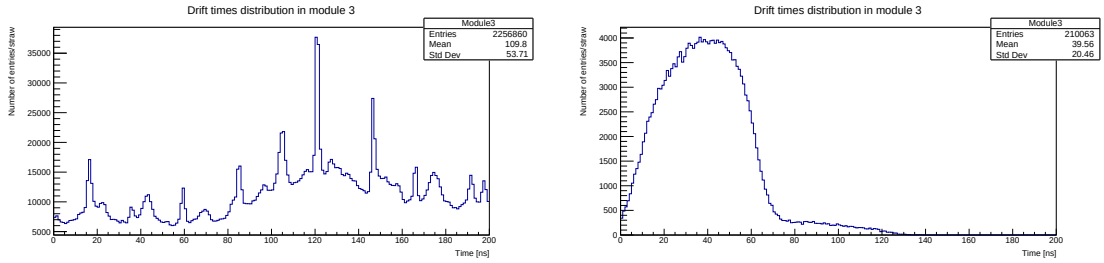

(a) Top module

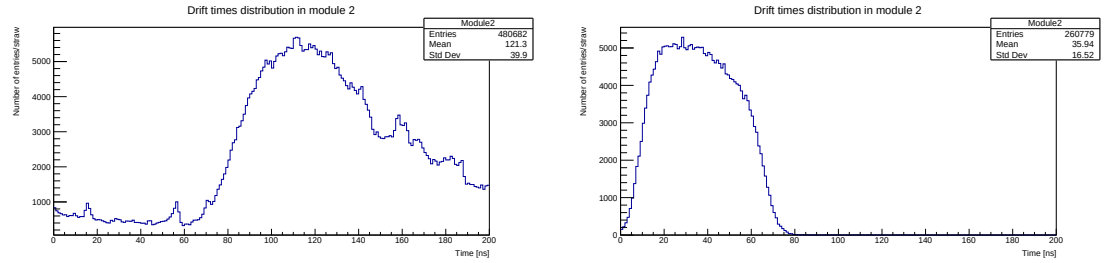

(b) Middle module

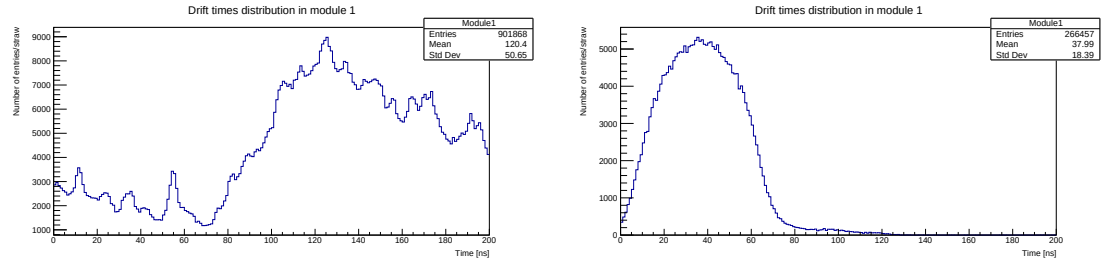

(c) Bottom module

Figure A.1.: Comparison of the drift time distribution of each module. The plots on the left-hand and the right-hand side show the status before and after applying the calibration, respectively.

A.3. Hits per Straw

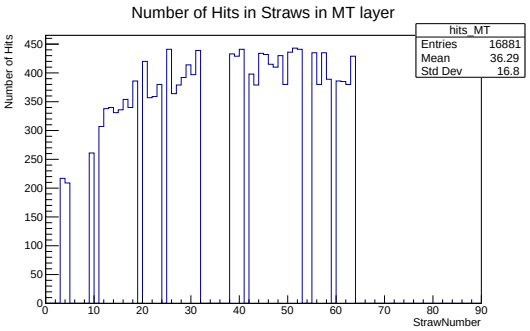

(a) Top layer, middle module

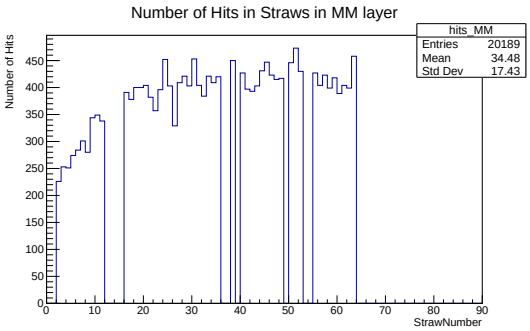

(b) Middle layer, middle module

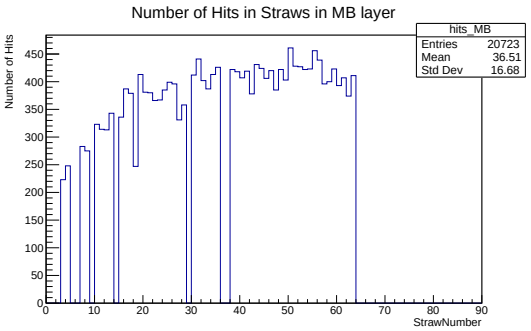

(c) Bottom layer, middle module

Figure A.2.: Hits per straw for each layer of the middle module

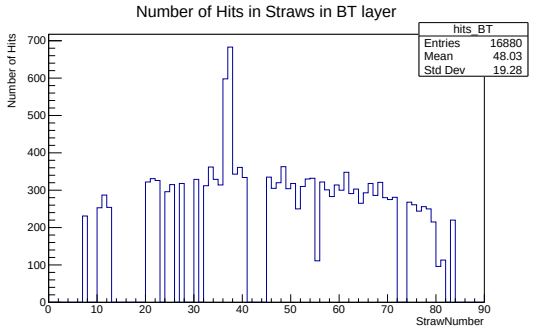

(a) Top layer, bottom module

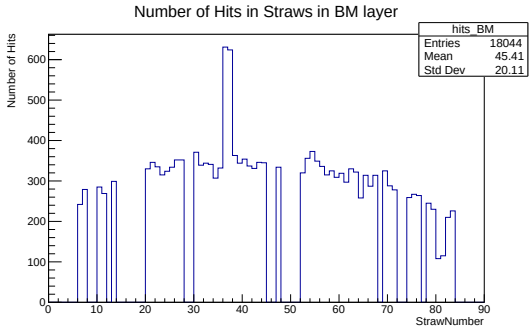

(b) Middle layer, bottom module

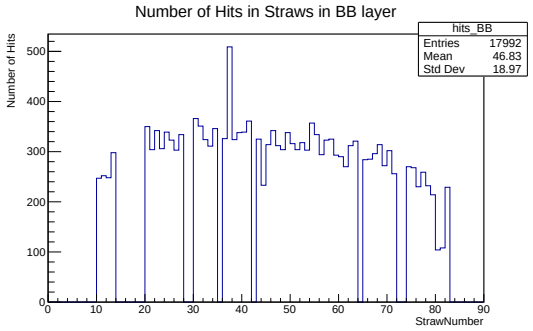

(c) Bottom layer, bottom module

Figure A.3.: Hits per straw for each layer of the bottom module

A.4. Efficiency and noise rate

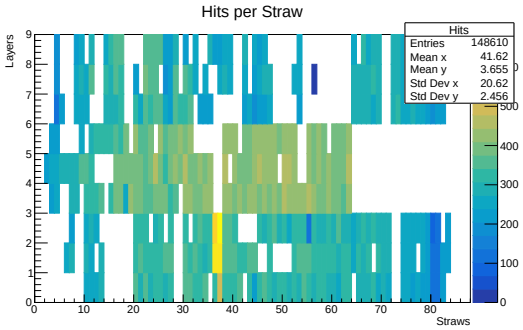

(a) Hits belonging to a reconstructed track

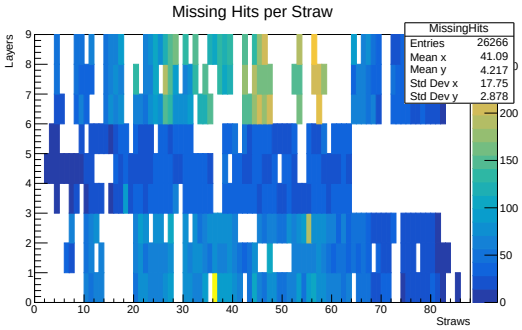

(b) Missing hits

Figure A.4.: Hits belonging to a reconstructed track and missing hits per straw

List of Figures

List of Tables

Bibliography

[1] University of Bonn. *E217 – STYX. Student Manual*. January 2025.

[2] Claus Grupen. *Einstieg in die Astroteilchenphysik*. Jan. 2018. ISBN: 978-3-662-55270-4. DOI: 10.1007/978-3-662-55271-1.